Electronic Supplementary Information for Galvanic Exchange in Colloidal Metal/Metal-Oxide Core/Shell Nanocrystals

Dominik Kriegner,[1,2,*] Mykhailo Sytnyk,[1,3,*] Heiko Groiss,[4,5] Maksym Yarema,[1] Wolfgang Grafeneder,[1] Peter Walter,[6] Ann-Christin Dippel,[6] Matthias Meffert,[5] Dagmar Gerthsen,[5] Julian Stangl,[1] and Wolfgang Heiss[1,3]

[1] *Institute of Semiconductor and Solid State Physics, Johannes Kepler University, Linz, Austria*

[2] *Department of Condensed Matter Physics, Charles University Prague, Czech Republic*

[3] *Materials Science Department (Materials for Electronics and Energy Technology), Friedrich-Alexander Universität Erlangen-Nürnberg, Energy Campus Nürnberg, 90429 Nürnberg*

[4] *Christian Doppler Laboratory for Microscopic and Spectroscopic Material Characterization, Center for Surface and Nanoanalytics (ZONA), Johannes Kepler University, Linz, Austria*

[5] *Laboratory for Electron Microscopy, Karlsruhe Institute of Technology, Karlsruhe, Germany*

[6] *Deutsches Elektronen-Synchrotron DESY, Hamburg, Germany*

[*] These authors contributed equally to this work

A. Synthesis of Sn nanocrystals

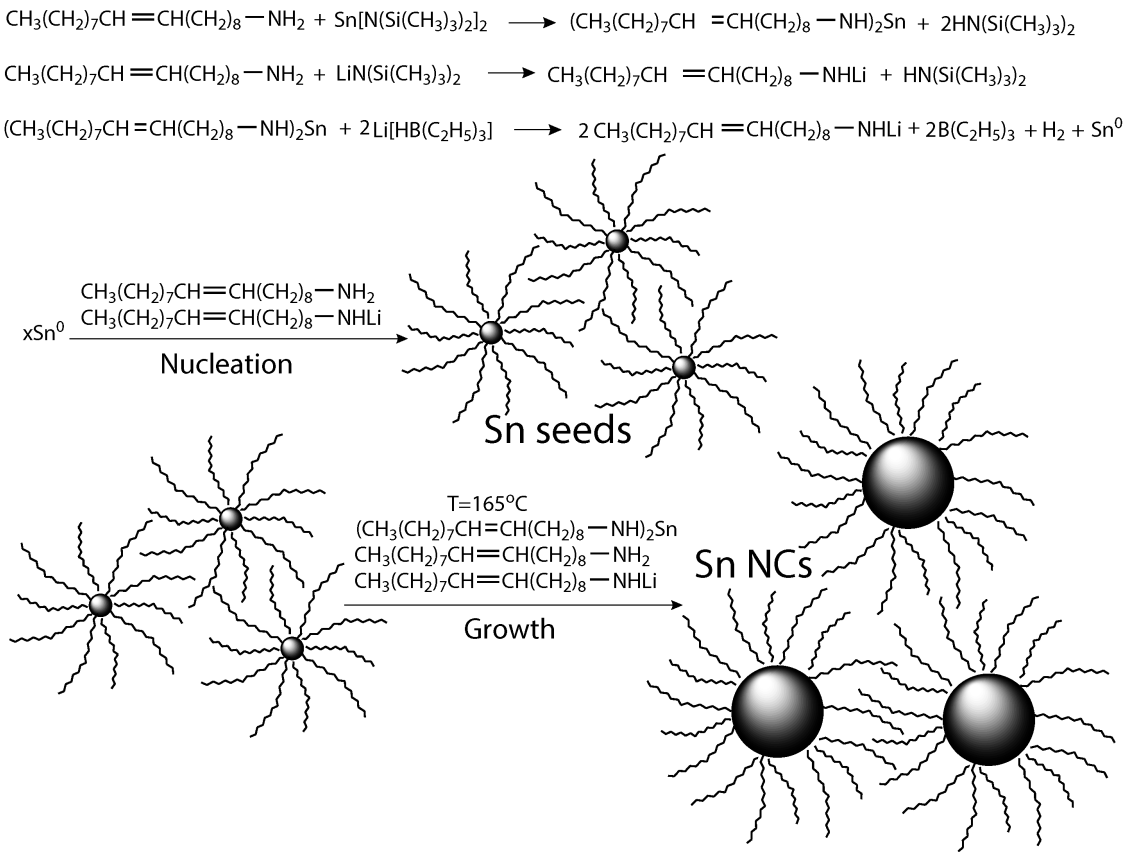

Supplementary Figure S1: Scheme of the Sn-nanocrystal synthesis. All reaction steps are shown, including the intermediate oleylamine compounds.

B. Technical details of the X-ray diffraction setup

A photograph of the X-ray powder diffraction setup at beamline P02.1 at Petra III/DESY is shown in Fig. S2. It shows the nanocrystalline samples placed in a Kapton capillary and indicates the X-ray beam as well as the hot nitrogen stream used for the heating of the samples. Detector images showing the raw 2D X-ray diffraction powder diffraction signal of the nanocrystals after synthesis and after the ex-situ galvanic exchange are displayed in Fig. S3. The primary beam was blocked by a beam-stop, whose absorption shadow can be seen in the center of the detector images. Diffractograms extracted from the images shown in Fig. S3 are shown in Fig. 1 (main text) together with a corresponding simulation performed with Rietveld analysis software MAUD. For the simulations a polynominal function was used to model the scattering background (mostly arising from air scattering for ex-situ

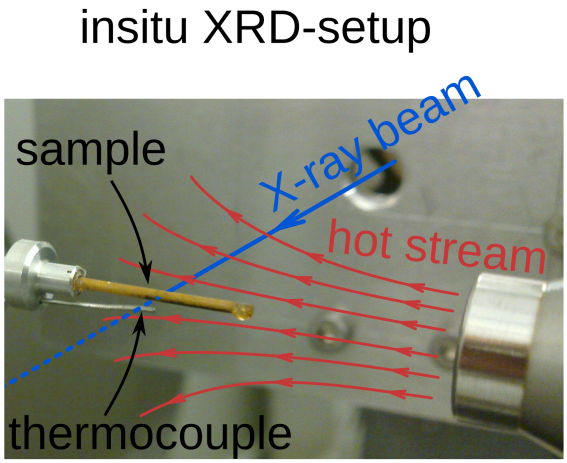

Supplementary Figure S2: Photograph of the X-ray diffraction setup used to monitor the galvanic exchange reaction in the nanocrystals. Shown is the Kapton capillary including the nanocrystals and precursor material for the galvanic exchange as well as the nitrogen stream used to heat the sample.

samples and dominated by scattering from the solvent for data acquired for in-situ samples). Diffraction from various sets of lattice planes up to a momentum transfer of $> 7\mathring{A}^{-1}$ were observed for the investigated Sn nanocrystals as can be seen in Fig. 1 (main text).

C. Monitoring the galvanic exchange by X-ray diffraction

The galvanic exchange reaction with Ag was monitored by continuously taking 2D powder diffraction patterns. This allowed us to resolve the process described in the main text with respect to time. The rate at which one can read the detector and the time needed to collect a decent signal is the only limiting factor for our method. Due to the low signal to background ratio due to the scattering from the solvent in the capillary we had to restrict the analysis of the in-situ measurements to the strongest peak. From the peak width we estimate the size of the nanocrystals. Hereby we neglect other influences on the peak width like strain, which were shown to be negligible by the full pattern fitting of ex-situ treated samples. Further we use the peak width of the strongest peak at lowest momentum transfer to be mostly strain insensitive. Several ex-situ treated samples were investigated which were treated at higher temperatures and for different times. The diffraction patterns of those samples treated with Ag TFA are shown in Figure S5. Figure S4 shows that the size of the nanocrystals is almost unchanged by the Ag TFA treatment. An overview of the treatments with Pt and Pd ions is shown in Figure S6. None of the treatments with Pt or Pd ions results in a change of the crystal structure.

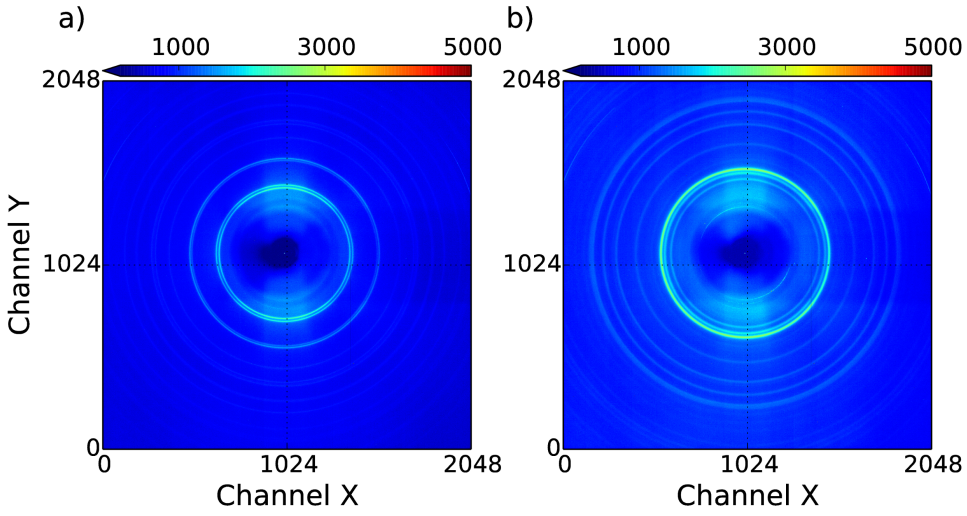

Supplementary Figure S3: Two dimensional X-ray powder diffraction patterns of Sn nanocrystals in (a) and Ag_xSn compound crystals in (b) recorded at beamline P02 in a single shot (1 sec acquisition time). From the 2D images a 1D powder pattern is generated by radial integration. In the center of the image a beam-stop blocks the primary beam and its absorption shadow can be seen.

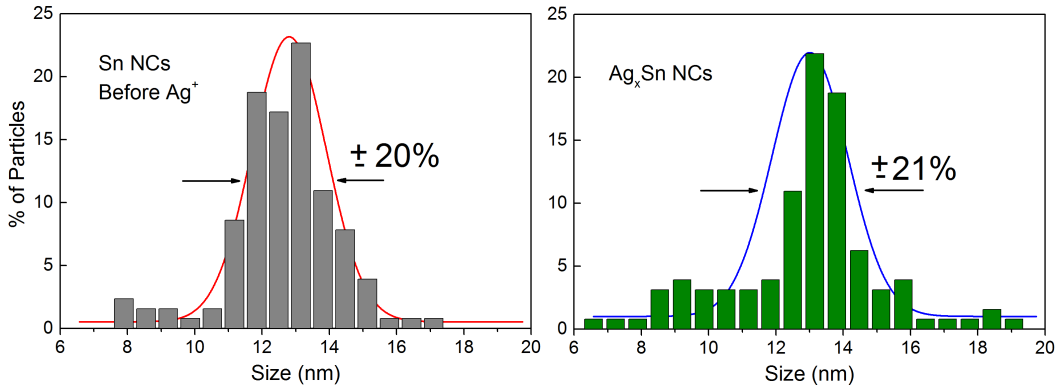

Supplementary Figure S4: Size histograms of the nanocrystals before (left) and after (right) the treatment with Ag TFA. The nanocrystal dimensions were extracted from TEM images as shown in the main text's Figure 1b.

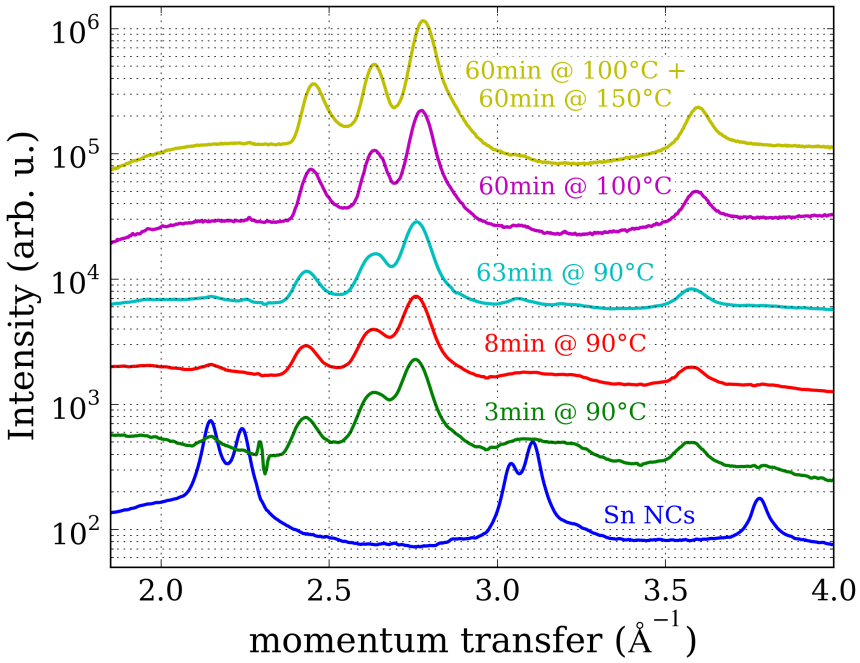

Supplementary Figure S5: Powder diffraction patterns of Sn nanocrystals subject to the described galvanic exchange reaction with Ag TFA for the listed times and temperatures. After the initial change of the Sn nanocrystals to the Ag_xSn phase extended treatment times and treatment at higher temperatures do not change the nanocrystals composition. The curves are vertically shifted for clarity.

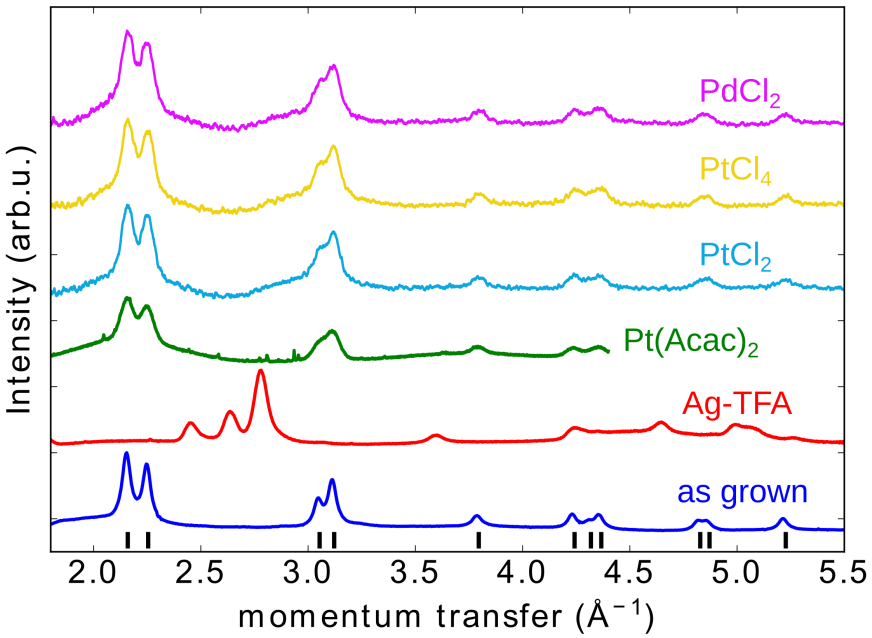

Supplementary Figure S6: Powder diffraction patterns of Sn nanocrystals subject to the unsuccessful galvanic exchange reaction with Pt and Pd ions. A treatment time and temperature of 60 min and 90°C was used in all cases. For comparison also the equal treatment using Ag TFA is shown which is the only reaction resulting in a change of the crystal structure. The curves are vertically shifted for clarity.

1. *Analysis of the time evolution*

To fit the time evolution shown in the main text's Figure 2 we use simple exponential decay functions as outlined below. The relative scattering volume V of the Sn and Ag-Sn phase during the exchange can be fitted by

$$V_{\mathrm{Sn}}(t) = \exp^{-(t/\tau_{\mathrm{Sn}})^n} \tag{1}$$

$$V_{\text{Ag-Sn}}(t) = 1 - \exp^{-\left(t/\tau_{\text{Ag-Sn}}\right)^n}, \tag{2}$$

with the parameters τ and n. The exponent n we set equal to one, because by fitting values close to 1 were found for both, the decay of Sn (n=1.09) and rise of the Ag-Sn signal (n=0.99). The used equations are equal to the Avrami equation. For both the decay of the Sn phase and the increase of the Ag-Sn phase we find very similar values of τ, which is obvious since the growth of the Ag-Sn phase occurs by transforming the existing Sn phase. The size of the growing Ag-Sn crystallites S can be similarly described by an exponential function in the initial stage of the reaction, however, we need to account for Ostwald ripening to be able to explain also evolution during the later stages in the reaction. We use the fact that the mean particle size during the ripening process is expected to increase with the third root of the time as in the Lifshitz-Slyozov-Wagner theory.

$$S(t) = -G\exp^{-t/\tau_S} + (K \cdot t + S_0^3)^{1/3} \tag{3}$$

The parameters G and τ_S account for the initial growth of the particles and the parameters S_0 (initial size) and K (ripening coefficient) describe the ripening. The contribution of the two terms to the time evolution is shown separately (as green and yellow lines) in Figure 2 in the main text.

D. Energy-dispersive X-ray spectroscopy and STEM investigations

The energy dispersive X-ray spectroscopy line-profile shown in Figure S7a was measured at a nanocrystal with diameter of 24 nm and presents the quantitative profiles before the separation of shell and core contributions. The shell is ∼3 nm thick, which leads to a core diameter of 19 nm. The line-scan contains a measuring point every nanometer, thus three spectra were taken across the shell without core contribution. Quantification of these spectra shows a change of the Ag-content from 0% at the surface to more than 20% at the shell/core interface. The O-content decreases in the opposite way, whereas the Sn-content changes only slightly. The average composition from these six spectra taken in the shell gives an average shell composition of 12% Ag 22% Sn and 66% O. This composition of the

shell has to be taken into account if the composition of the core is determined. The shell signal can be subtracted because of the linear relation of composition and peak intensity. The average shell contribution was than subtracted weighted (ratio of the electron-beam path-length through the shell/core) for the inner part of the dot between ±9 nm. This leads to a flat composition profile, which indicates a homogeneous core composition, which is shown in Figure S7b between the two dashed lines. The average composition of the core obtained from the six nearest points to the nanocrystal center gives (with O-content set to zero) a composition of 68% Ag and 32% Sn, with an estimated uncertainty of 5%. A similar, but different measurement at a smaller nanocrystal is shown in Figure S7c,d. This particle has a diameter of 19 nm and a shell thickness of ~ 3 nm. Because this measurement was less accurate (low signal/noise ratio of the smaller nanocrystal) and a measuring point distance of 2 nm (to avoid beam damage), the average shell composition could not be calculated. Thus the shell was assumed to be composed of 15% Ag 20% Sn and 65% O. This composition is similar to the shell composition found in the previous measurement but was slightly adapted to minimize the artifacts of the shell subtraction. Figure S7c shows the profile before the shell correction. The result of the shell subtraction can be seen in Figure S7d. Due to the lower accuracy of the measurement the path-length ratio between core and shell near the core/shell interface is very sensitive to small changes. This leads to an artifact close to this interface, which yields negative O-contents and unrealistically high Ag-values. Near the center of the particle the measurement is less sensitive on the core/shell ratio, thus the measurement and correction lead to more accurate results. The mean of the three center points give a core composition of 81% Ag and 19% Sn. Thus, smaller dots have definitely a higher Ag-content compared to the larger ones, and reveal a composition which corresponds to the Ag_4Sn phase.

Lewis Base	β	Ligands
Hard	< 5	Ac^-, $ACAC^-$, OH^-,NH_2^-, NH_3, NO_3^-, Cl^-, H_2O, $\mathbf{RNH}_2$, OA
Borderline	$5 \sim 6$	Br^-, $C_6H_5NH_2$, N_3^-, NO_2^-, SO_2
Soft	> 6	I^-, $S_2O_3^{2-}$, R2S(Se,Te), RS(Se,Te)H, R3P, R3As, (RO)3P, TOP

Supplementary Table S1: Basicity (β) of common Lewis bases (ligands) evaluated from the instability constants of the metal ion complexes [S1, S2]. Abbreviations Ac^- and $ACAC^-$ are acetat and acetylacetonate, respectively.

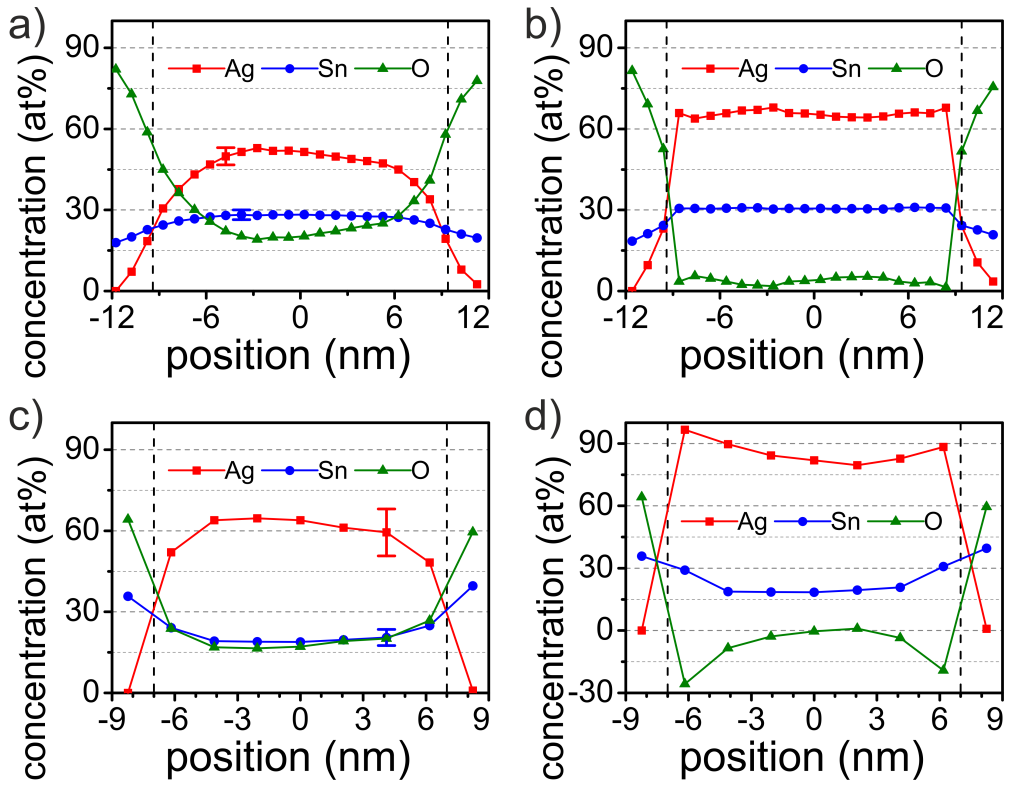

Supplementary Figure S7: (a) depicts the atomic concentration calculated from the EDXS-line scans of a 24 nm dot. The concentrations are the average compositions along the electron path, which penetrates in the center of the dot (between the indicated shell/core interface) the shell and core. (b) shows separated profiles, which were calculated by weighted subtraction of the shell signal part. The homogenous core composition can be seen. The representative error bars for the Ag- and Sn-concentrations define the 2σ confidence levels of the analyzed peaks. (c) and (d) show similar panels for a measurement at a smaller dot with an diameter of 19 nm.

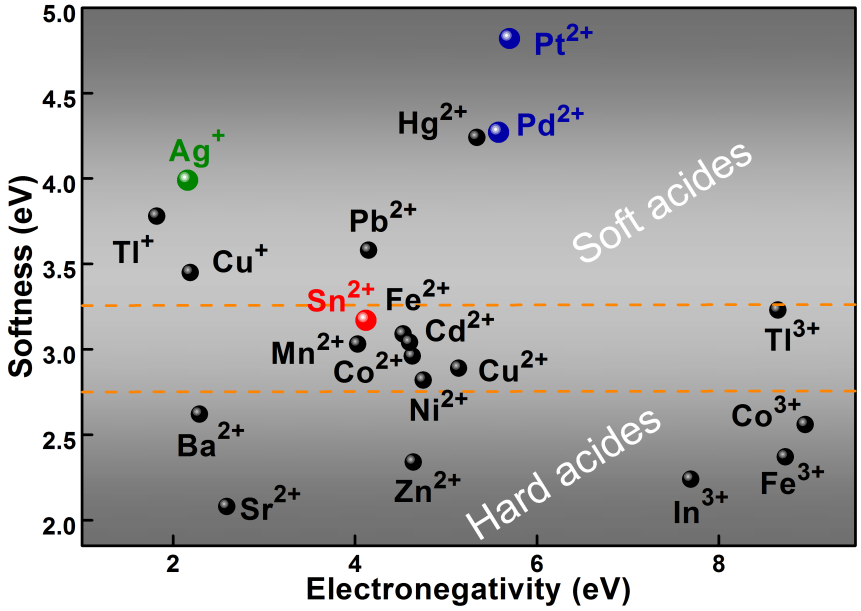

Supplementary Figure S8: Level of acidity of the common Lewis acids (metal cations) calculated by using electronegativity, ionization potential and ionic radius of the ions [S1, S2].

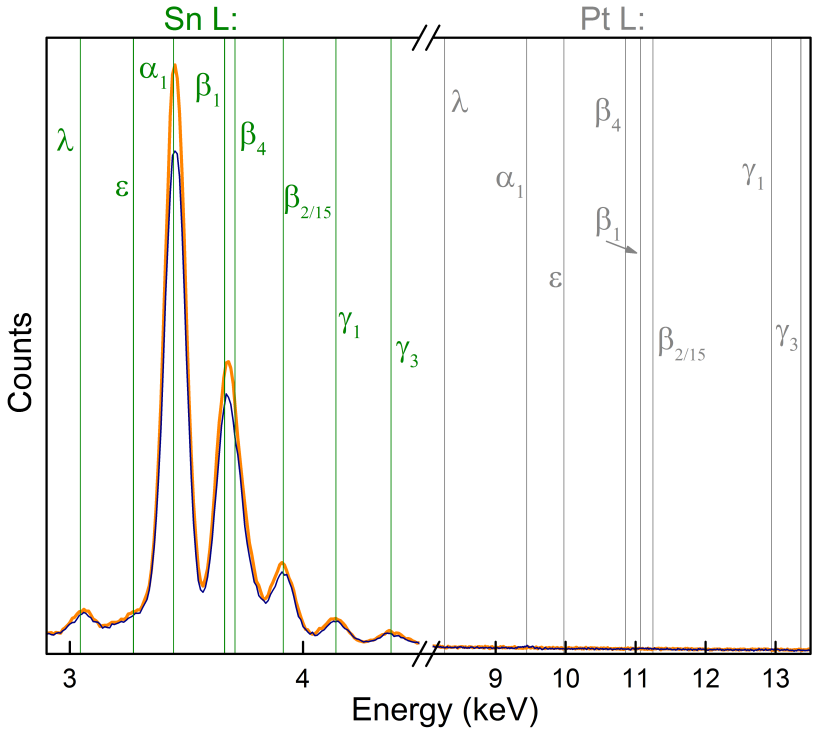

Supplementary Figure S9: Energy dispersive X-ray spectroscopy data of Sn nanocrystals treated with Pt^{2+}. Shown is the spectrum of both, the as grown (orange) and treated Sn nanocrystals sample. We could not find any significant trace of Pt-L lines, whereas the Sn-L lines are observed very clearly in both samples. The shown measurements were performed in a scanning electron microscope with an electron energy of 30 keV.

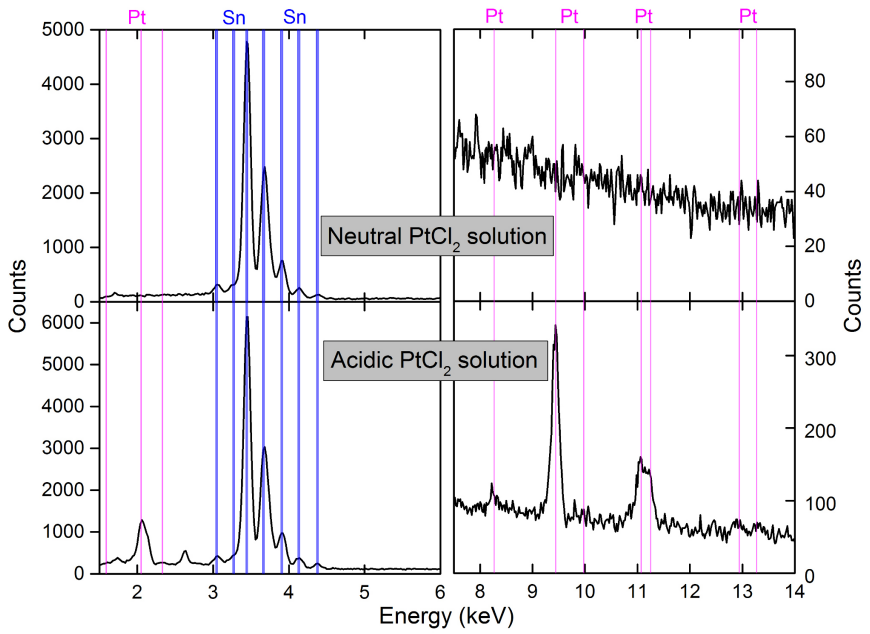

Supplementary Figure S10: Energy dispersive X-ray spectroscopy data of bulk Sn shots treated with Pt^{2+}. Shown are the spectra for treatment in neutral and acidic solutions. While for the treatment in neutral water only Sn lines can be detected we find strong signal of Pt after the treatment in acidic solutions. The shown measurements were performed in a scanning electron microscope with an electron energy of 30 keV.

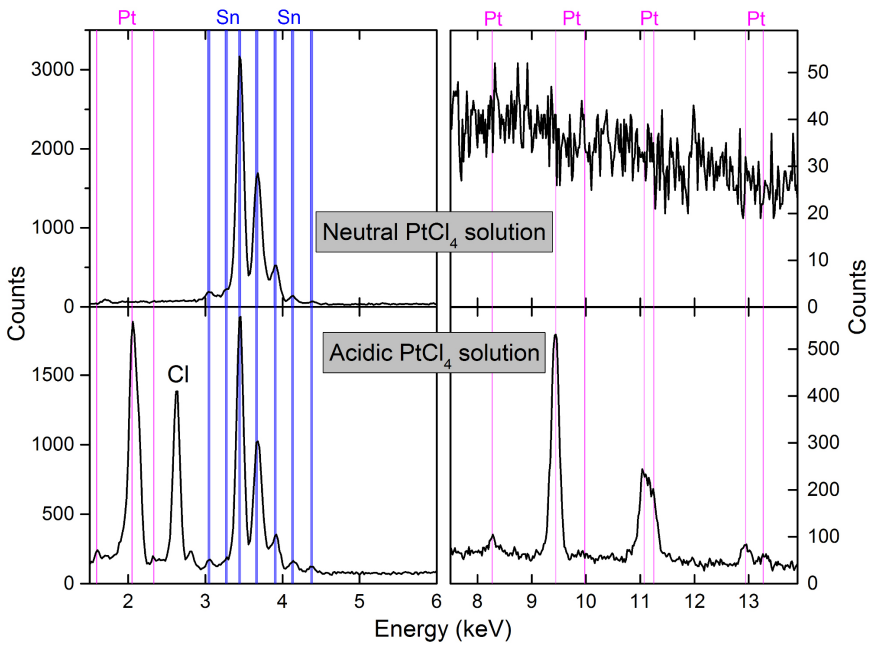

Supplementary Figure S11: Energy dispersive X-ray spectroscopy data of bulk Sn shots treated with Pt^{4+}. Shown are the spectra for treatment in neutral and acidic solutions. While for the treatment in neutral water only Sn lines can be detected we find strong signal of Pt after the treatment in acidic solutions. The shown measurements were performed in a scanning electron microscope with an electron energy of 30 keV.

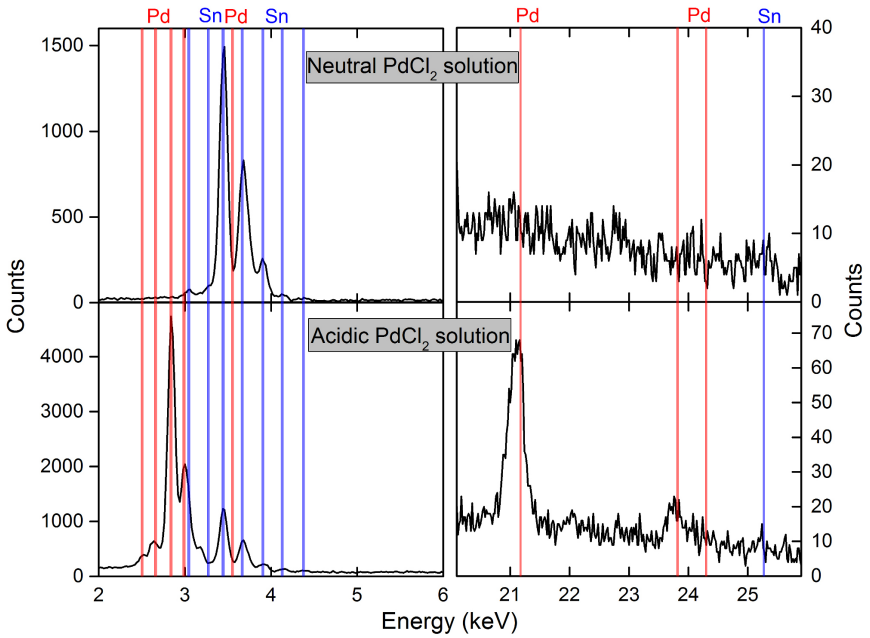

Supplementary Figure S12: Energy dispersive X-ray spectroscopy data of bulk Sn shots treated with Pd^{2+}. Shown are the spectra for treatment in neutral and acidic solutions. While for the treatment in neutral water only Sn lines can be detected we find strong signal of Pd after the treatment in acidic solutions. The shown measurements were performed in a scanning electron microscope with an electron energy of 30 keV.

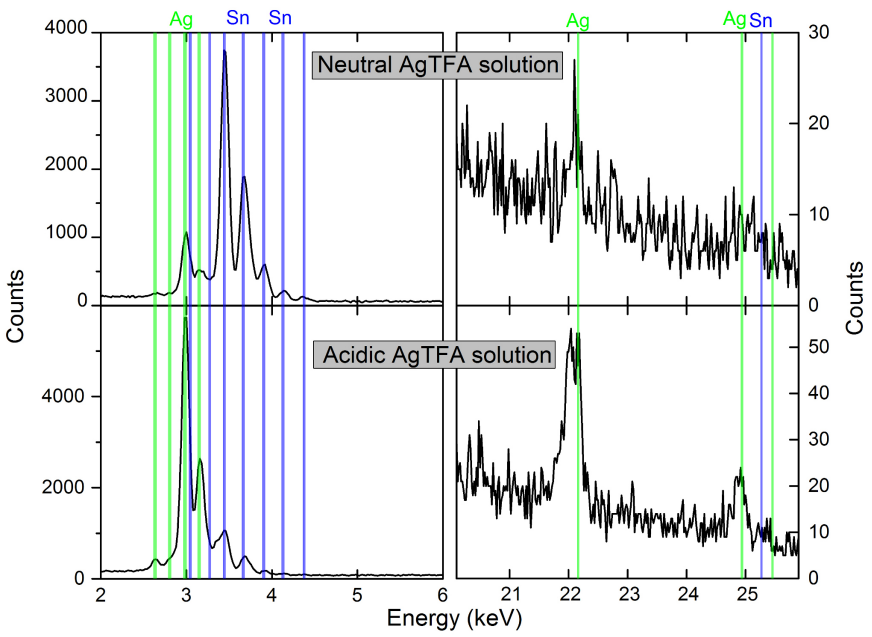

Supplementary Figure S13: Energy dispersive X-ray spectroscopy data of bulk Sn shots treated with Ag^+. Shown are the spectra for treatment in neutral and acidic solutions. In both cases Sn and Ag lines can be detected, the Ag contribution is, however, larger for treatment in acidic solution. The shown measurements were performed in a scanning electron microscope with an electron energy of 30 keV.

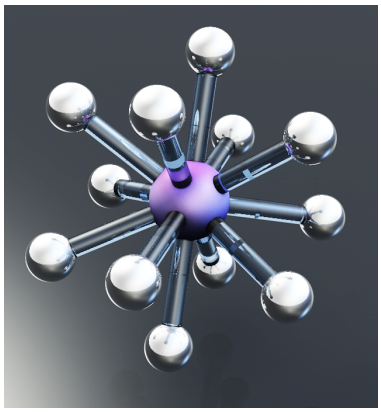

Supplementary Figure S14: Sketch showing the 12-fold coordination of the Sn atoms (central ball) in the Ag_4Sn structure.

[S1] M. Misono, E. Ochiai, Y. Saito, and Y. Yoneda, J. Inorg. Nucl. Chem. **29**, 2685 (1967).

[S2] J. Zhang, Y. Tang, K. Lee, and M. Ouyang, Science **327**, 1634 (SI) (2010).